Physical Origins of the Transient Absorption Spectra and Dynamics in Thin-Film Semiconductors: The Case of BiVO$_4$

Jason K. Cooper,*[†,‡] Sebastian E. Reyes-Lillo,[§,∥,⊥] Lucas H. Hess,[†] Chang-Ming Jiang,[†] Jeffrey B. Neaton,[§,∥,#] and Ian D. Sharp*[†,‡,¶]

[†]Joint Center for Artificial Photosynthesis, [‡]Chemical Sciences Division, and [§]Molecular Foundry, Lawrence Berkeley National Laboratory, Berkeley, California 94720, United States

[∥]Department of Physics, University of California, Berkeley, Berkeley, California 94720, United States

[⊥]Departmento de Ciencias Físicas, Universidad Andres Bello, Santiago 837-0136, Chile

[#]Kavli Energy NanoSciences Institute at Berkeley, Berkeley, California 94720, United States

[¶]Walter Schottky Institut and Physik Department, Technische Universitat München, 95748 Garching, Germany

Ⓢ *Supporting Information*

ABSTRACT: Transient absorption (TA) spectroscopy is uniquely suited for understanding kinetic processes initiated by light over vast ranges of time. In combination with white light probes, the recorded differential absorption spectra can contain spectroscopic signatures characteristic of specific charge carrier population densities. However, disentangling the often-complex and convoluted spectra is made challenging without robust analysis methods relating the underlying physical mechanisms to the spectral components. In this work, we address the origin of the transient spectra of a model system of emerging solar energy harvesting materials using a monoclinic BiVO$_4$ thin film. Using ground-state optical properties of the semiconductor, we find the main derivative-like spectral response to be related to shifting and broadening of oscillators, rather than specific carrier-related transitions. However, by using the Drude optical model of free carriers, we also identify the transient response related to free-hole density. Importantly, sample heating from the optical pumping, which begins at ~10 ps and plateaus by ~200 ps, dominates the overall spectral response at longer times. On the basis of a physical model of the spectral response, a kinetic model is developed that describes the pump power dependence of the free-hole density, as well as the temporal evolution of the spectral changes associated with shifting and broadening of oscillators. First-principles density functional theory calculations are used to rationalize experimental measurements. This comprehensive approach to analyzing and modeling the TA spectra offers a generalizable basis for understanding the complex pump−probe data, reveals thermal heating artifacts that are frequently erroneously assigned to long-lived photocarriers, and offers a path to eliminating ambiguity in analysis of photocarrier dynamics in solid-state systems.
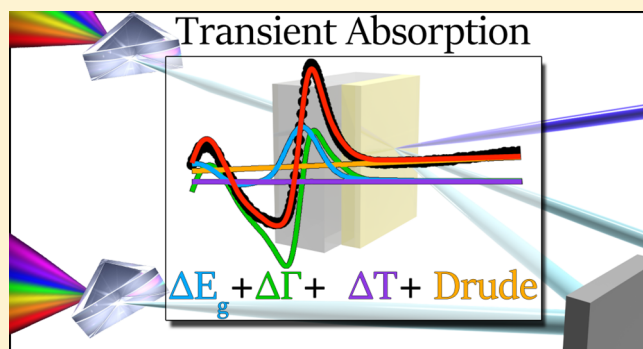
1. INTRODUCTION

Transient absorption (TA) spectroscopy is a powerful method for characterizing photocarrier dynamics in semiconductors over the full range of their natural time scales, which can extend from the attosecond regime[1] to beyond seconds.[2] In addition, this pump−probe method can be applied to materials that do not exhibit efficient photoluminescence (PL), which makes it particularly attractive for the study of transition-metal oxide and oxynitride semiconductors. Such materials are actively investigated for photoelectrochemical energy conversion but are rich in defects and often possess indirect band gaps. Because solar energy conversion efficiencies obtained from these materials typically fall far short of theoretical limits, it is especially important to understand loss mechanisms associated with photocarrier relaxation, trapping, and recombi-

nation. Despite the promise of TA for interrogating such processes, measured spectra tend to be characterized by broad and convoluted spectral features, the origins of which are poorly understood. In the absence of robust physical assignments of spectral components, kinetic models based on their temporal evolution contain significant ambiguity in terms of physical mechanistic insights.

In many respects, TA is analogous to the suite of quasi-steady-state modulation spectroscopies in which continuous-wave probe light is used to measure changes of the optical response as the sample is perturbed by a periodic stimulus

(e.g., optical excitation, temperature, pressure, electrochemical potential, etc.). In such experiments, the resulting dominant signal can be described by first, third, or a mixture of first and third derivatives of the complex dielectric function with respect to energy due to shifting transition energies, changing oscillator strengths, or energetic broadening of transitions. Primary spectral features occur at critical point transitions, such as direct valence to conduction band excitations.[3] The connection between traditional modulation spectroscopies and time-resolved pump−probe experiments was recently highlighted by the work of Yang et al., who analyzed time-resolved photoreflectance data of p-type $GaInP_2$ to characterize interfacial charge-transfer processes and transient surface electric fields.[4] This is in contrast to the traditional perspective utilized in molecular spectroscopy, where negative differential absorption (i.e., "bleach") features are considered to arise from depopulation of the ground state, whereas positive differential absorption (i.e., "induced" or "stimulated absorption") is frequently associated with excited-state transitions from nonequilibrium populations of electronic states generated by the pump pulse.

In this work, we consider the underlying processes that give rise to TA signals in thin-film semiconductors and provide a physical model for the spectral response, as well as its kinetic evolution. A description of the differential absorption spectra, obtained by considering both reflection and transmission, is based on the ground-state optical properties of the semiconductor. This analysis is applied to $BiVO_4$, which is currently the best performing transition-metal oxide photoanode material, despite current gaps in understanding of the mechanisms governing photocarrier trapping and recombination. On the basis of the optical properties of the material, combined with analysis of known mechanisms for band edge broadening, band gap alterations, and free-carrier absorption, the differential excited-state spectrum at ultrafast time scales can be completely described. Structural, electronic, and vibrational properties are obtained using density functional theory (DFT) calculations (see Supporting Information for details) and rationalize our measurements. We find that nonequilibrium phonon populations (i.e., thermal effects), rather than nonequilibrium charge carrier populations, dominate the spectral response at time delays >100 ps. Modeling of the kinetic evolution of specifically assigned spectral features provides new physical insights into the life cycles of photogenerated carriers. The concepts described here can be applied as a framework for understanding TA spectra and photocarrier dynamics in the broad range of solid-state systems including emerging semiconductors envisioned for the next generation of solar fuel systems.

2. EXPERIMENTAL SECTION

2.1. Thin-Film Sample Preparation. Spin-coated bismuth vanadate thin films were prepared by adapting a literature procedure.[5,6] In a typical deposition, 15 mL of a 0.2 M solution of bismuth(III) nitrate pentahydrate (Sigma-Aldrich, ≥98%) in acetylacetone (Sigma-Aldrich, ≥99%) and 100 mL of a 0.03 M solution of vanadium(IV)-oxy acetylacetonate in acetylacetone were prepared separately and sonicated for 10 min. Next, the two solutions were mixed together and sonicated for an additional 5 min. Approximately 1−1.2 mL of the resulting solution—enough to homogeneously cover the substrate surface—was filtered with 0.45 μm nylon filters (Thermo Scientific) and dispensed

onto a 4 in. diameter fused silica wafer. Prior to deposition, the fused silica substrate was thoroughly washed with isopropanol and with detergent and deionized water, dried with a nitrogen gun, and treated for 10 min in an ozone cleaner (Jelight model 42). The substrate, with the precursor solution covering its surface, was then spun twice in a row at 1000 rpm for 6 s on a Laurell Technologies spin coater with an acceleration rate of 150 rpm/s. After this spin-coating cycle, the substrate was annealed for 10 min at 500 °C in a muffle furnace. This procedure (i.e., spin-coating followed by short annealing) was repeated nine times. After the final spin-coating cycle, the substrate was annealed for 2 h at 500 °C to achieve a final thickness of ∼50 nm.

2.2. TA Spectroscopy. Optical pump−optical probe TA spectroscopy was performed using a Coherent Libra (Coherent, CA, USA) laser with pulse width of 100 fs and repetition rate of 1 kHz. A portion of the output was coupled to a Coherent OPerA Solo optical parametric amplifier, which generated the 350 nm laser pump pulse. The pump beam diameter was 0.3 mm at the sample, and the pulse energy was tuned using a graded neutral density filter. The supercontinuum white light probe was generated using a CaF_2 crystal, into which a portion of the 800 nm output from the Libra laser was coupled. The incident angle of the probe beam was approximately 20° with respect to the sample surface normal. An Ultrafast Systems (Sarasota, FL, USA) TA measurement system was used and included two fiber-coupled grating spectrometers with Si complementary metal-oxide semiconductor detector arrays for analysis of the ∼315−800 nm spectral range. The setup was modified such that one detector was used to detect the differential transmission (dT) signal and the other was used for simultaneous collection of the differential reflection (dR) signal. The differential signal was calculated by dT, $dR = \log(I_{pumped}/I_{unpumped})$. The differential absorption (dA) signal was calculated from the dT and dR spectra using eq S1, in the Supporting Information. Fitting of the dA spectra was accomplished using in-house written MATLAB code and the built-in nonlinear least-squares solver lsqcurvefit. The sample absorption coefficient at 350 nm (α_{350nm}) and thickness (L) were $\alpha_{350nm} = 2.96 \times 10^5$ cm^{-1} and $L = 53$ nm, respectively.

Temperature-dependent ultrafast transient transmission (dT) was collected with the sample mounted in a closed-cycle He cryostat (Janis Research Company, Wilmington, MA, USA) equipped with a temperature controller (model 335, Lake Shore Cryotronics, Inc., Westerville, OH, USA). The temperature range investigated was from 11 to 373 K. For practical reasons, we were unable to co-collect dR using the cryostat employed for these measurements. The 453 nm probe wavelength was chosen to display the data, as it is both sensitive to modulations in the position of the derivative feature as well as it minimizes the signal from nonoscillatory components.

2.3. Steady-State Optical Spectroscopy. Variable-angle spectroscopic ellipsometry (VASE) measurements were conducted using an M-2000 ellipsometer with extended near-infrared (NIR) range by J.A. Woollam Co., Inc (Lincoln, NE, USA). Data fitting was conducted with the CompleteEASE software. The optical model used has been reported previously.[7] Briefly, a fit of the Ψ and Δ data was performed using a three-oscillator model to account for the indirect, direct, and UV regions of the absorption spectrum. The indirect gap was modeled with a Cody−Lorentz oscillator,

which includes a component to describe the Urbach tail associated with disorder-induced subgap absorption. The direct gap was modeled with PSemi-M0, which is effective for modeling the E_0 critical point in direct semiconductors such as CdO[8] and ZnO.[9] The remaining UV absorption was fit with a PSemi-Tri oscillator.

Temperature-dependent transmission and reflection spectra were collected using a SolidSpec-3700 UV−VIS−NIR spectrophotometer. The sample was positioned at 25° with respect to the indecent light. Temperature control was achieved through use of a closed-cycle liquid helium cryostat (Janis Research Company, Wilmington, MA, USA), and the temperature range studied was from 298 to 340 K.

2.4. Computational Methods. First-principles DFT calculations were performed with the Vienna Ab initio Simulation Package (VASP).[10] Effective masses and phonon frequencies were computed using the generalized gradient approximation (DFT−GGA) of Perdew, Burke, and Ernzerhof,[11] Γ-centered k-point grids, and projected augmented wave pseudopotentials with 5, 5, and 6 valence electrons for Bi, V, and O, respectively.[12,13] Selected structural calculations were performed with the Heyd−Scuseria−Ernzerhof (DFT−HSE)[14] hybrid functional to properly reproduce the structure of monoclinic BiVO$_4$ (see Supporting Information). Full structural relaxations of lattice parameters, volume, and internal atomic coordinates were performed until forces were smaller than 1 meV/Å. Effective masses and band structure calculations were computed for monoclinic BiVO$_4$ using a plane-wave energy cutoff of 450 eV and a $4 \times 4 \times 4$ k-point grid. Phonon eigenfrequencies and eigenvectors were calculated within the harmonic approximation using density functional perturbation theory.[15] Phonon calculations were performed for the reference tetragonal BiVO$_4$ structure using DFT−GGA, the primitive unit cell (12 atoms), and a finer $8 \times 8 \times 6$ k-point grid. The selected phonon modes were plotted using VESTA.[16]

3. RESULTS AND DISCUSSION

3.1. Transient Reflection, Transmission, and Absorption Spectra. Development of a physical model that describes TA data relies on the accurate measurement of the spectrum. In common practice, the differential transmission (dT) signal is used as an approximation of the differential absorption (dA) signal by comparing the pumped and unpumped transmission intensities of the probe light according to d$A = -\log(I_{\mathrm{pumped}}/I_{\mathrm{unpumped}})$. For the case of molecular and nanoparticle systems in solution, d$A = -$dT. For solid-state systems, however, this approach relies on the implicit assumption that the differential reflection (dR) is negligible. This assumption is, in general, not valid. In reality, a variety of physical processes contribute to changes of reflectivity under photoexcitation. Therefore, in the present work, we simultaneously record both dT and dR signals, which enables calculation of dA, as described in the Supporting Information. Figure 1 shows the measured dT and dR spectra, together with the calculated dA spectrum, obtained from a 50 nm thick film of BiVO$_4$ on a fused silica substrate.

The dT signal is characterized by a derivative-like line shape with a negative peak at 460 nm and a broad negative background with gradually increasing amplitude at wavelengths greater than ∼525 nm. The dR signal is also characterized by a derivative-like spectrum, but with a sharper line shape and a negative peak at 464 nm. A gradually decreasing dR is observed at wavelengths extending beyond 500 nm. Although the
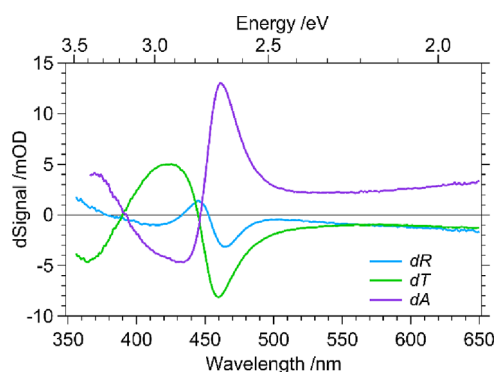
Figure 1. Transient differential reflection (dR), transmission (dT), and absorption (dA) of BiVO$_4$ (50 nm on fused silica) at 430 fs pump−probe delay. Excitation wavelength: 350 nm, power: 600 nJ/pulse, approximate beam diameter: 0.3 mm.

amplitude of dR is smaller than dT, its contribution to dA is not negligible (Figure 1). In particular, dA exhibits a slight redshift of the peak to 462 nm, as well as different relative weights of the component spectral features.

3.1.1. Electronic Contributions. To date, there have been several studies examining the TA of BiVO$_4$. A positive dA signal at wavelengths between 500 and 900 nm has consistently been assigned to photoexcited hole absorption (commonly as trapped holes) through a combination of in situ methods, including use of chemical scavengers and applied electrochemical bias.[17−22] The negative spectral response around 440 nm has been assigned to ground-state bleaching.[19−21] Finally, the large positive response around 475 nm has been generally assigned to charge carrier absorption[19] and more specifically to hole absorption.[21] As described below, our analysis confirms the first of these assignments, but indicates an alternative origin for the dominant spectral features at wavelengths shorter than 500 nm.

In previous reports, we characterized BiVO$_4$ as having an indirect band gap of 2.5 eV (496 nm) with a higher lying direct transition at about 2.7 eV (459 nm).[7,23] In relation to these ground-state optical properties, the dominant spectral features observed in transient spectra of BiVO$_4$ are generally centered around the direct transition. This is consistent with modulation spectroscopy methods, where first- or third-derivative line shapes are expected near critical point energies, such as direct transitions. In particular, third-derivative line shapes are a consequence of a change in the oscillator strength and/or energetic broadening of the oscillator associated with a particular optical transition, whereas first-derivative line shapes are associated with an energetic shift of such an oscillator.[24]

To further explore the relationship between TA and ground-state optical properties, we have examined the first and third derivatives of the optical constants of the material, which were obtained by VASE. In Figure 2a,b, n and κ are compared, respectively, to the first and third derivatives of n (dn/dE and d^3n/dE^3) and κ (dκ/dE and d$^3\kappa$/dE^3) as well as to the dR and dA spectra. Broadly speaking, the dR spectrum is in good agreement with d^3n/dE^3. Under photoexcitation, the built-in electric field is modulated from a maximum in the dark to near flat band under illumination, thereby accelerating free carriers within the material.[25] The accelerated carriers no longer have translational symmetry, and thus momentum conservation governing vertical excitations in k-space is relaxed, resulting in allowed nonvertical excitations. This manifests as a third-
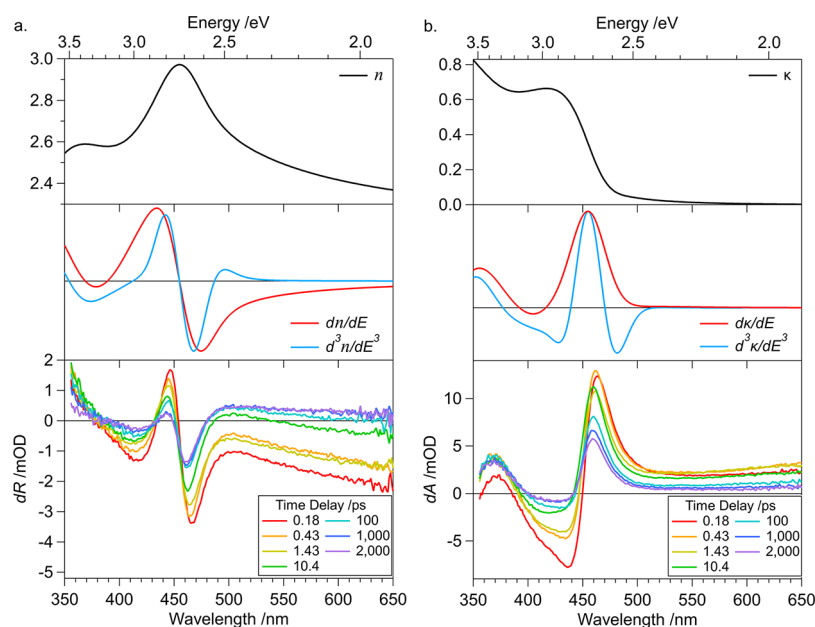
Figure 2. (a/b Top) Refractive index (n) and extinction coefficient (κ), respectively, determined by VASE for BiVO$_4$. (a/b Middle) d/dE and d^3/dE^3 spectra. (a/b Bottom) dR and dA, respectively, shown for a series of time delays. Pump = 350 nm, 600 nJ.

derivative line shape in the difference spectrum. Because band bending is greatest at the surface, the reflection spectrum is expected to be more sensitive to this effect than the transmission spectrum.

The dA spectrum is better represented by dκ/dE, which is related to shifting of the critical point transition energies of the photoexcited state.[24] Band edge shifts can be the result of multiple factors, one of which is band gap renormalization, in which the increase in photoexcited free-carrier density reduces the magnitude of the band gap through exchange−correlation effects.[26] This effect is well known, always leads to a reduction of the optical transition energy, and has been studied in a broad range of semiconductor systems.[27] However, additional phenomena may also contribute to changes in the band gap (ΔE_g), thereby complicating quantitative analysis of photo-carrier-induced renormalization. Optical excitation can induce changes in lattice constant over different length scales via lattice heating, strain field generation, electron/phonon coupling, and/or polaron formation. For example, polarons (both large and small) produce a local lattice distortion around the excited carrier, which slightly affects the band energetics. Polaronic band gap modulation has been previously reported in GaAs, where the magnitudes of the exchange−correlation and polaronic effects were found to be similar.[28]

To recreate the ΔE_g component of the dA spectrum, we first consider a uniform shift of the ground-state extinction coefficient (κ). We calculate the time-dependent extinction coefficient difference spectrum (d$\kappa_{\Delta E_g}(E,t)$), defined by

$$\mathrm{d}\kappa_{\Delta E_g}(E, t) = \kappa(E - \delta(t)) - \kappa(E) \tag{1}$$

where $\delta(t)$ is the time-dependent energetic shift of κ. The spectral response of this component at several shift energies between 1 and 40 meV is given in Supporting Information Figure S1a. Although the general shape of the spectrum is only slightly affected by the magnitude of the shift, the amplitude of the spectrum is a strong function of $\delta(t)$.

Free carriers provide an additional contribution to the TA response, which often manifests as an absorption feature that smoothly increases into the NIR spectral range. For the case of metal oxides, the free-carrier lifetime tends to be very short because of self-trapping, defect trapping, or recombination. As such, the free-carrier response signal is expected to only persist for short times and to be most evident in the NIR region of the spectrum. Upon photoexcitation with the pump laser—and prior to defect trapping, self-trapping (i.e., polaron formation), or recombination—a nearly instantaneous increase of the free-carrier concentration occurs. To a first approximation, the optical absorption associated with the resulting nonequilibrium concentration of free carriers can be described by the Drude model, in which the extinction coefficient (κ_{Drude}) is given by the imaginary part ($\mathfrak{I}$) of the complex function

$$\kappa_{\mathrm{Drude}}(E) = \mathfrak{I}\left(\sqrt{1 - \frac{\hbar^2}{\varepsilon_0 \rho(\tau E^2 + i\hbar E)}} \right) \tag{2}$$

where τ is the scattering time, E is the photon energy, and ρ is given, in time-dependent form, by eq 3

$$\rho(t) = \frac{m^*}{N(t)q^2\tau} = \frac{1}{q\mu N(t)} \tag{3}$$

with free-carrier density (N), effective mass (m^*), and the carrier mobility (μ). Here, we express the free-carrier density as a function of time (i.e., the pump−probe delay time) and assume that m^* and τ are approximately time-independent. Because the electrical mobility of BiVO$_4$ is governed by small polaron hopping, the value of m^* associated with the free-carrier-related Drude signal will differ from values obtained via steady-state transport measurements.

The Drude spectral component was compared to the dA response obtained 0.43 ps after excitation (350 nm pump with 600 nJ pulse energy) over the probe wavelength range of 350 to 1600 nm. At this pulse energy and density, the expected carrier density, based on the sample absorption coefficient and thickness, is 5.87×10^{19} cm^{-3}. We obtain the best agreement with $\mu = 0.85 \pm 0.05$ cm^2 V^{-1} s^{-1} and $m^* = 0.8 \pm 0.05 m_e$, Supporting Information Figure S2a. With these parameters, $\tau =$

0.39 fs. The diffusion length is calculated to be 110 nm by approximating the lifetime based on the e^{-1} decay of the Drude response, which is 135 ps. This finding is consistent with previous reports of the hole diffusion length of ∼100 nm.[29,30] Using time-resolved terahertz spectroscopy at injection levels up to 2.5×10^{18} cm^{-3}, Butler et al. reported the free-carrier mobility to be 200 cm^2 V^{-1} s^{-1} through fitting with $m_e^* = 0.3$ and $\tau = 35 \pm 10$ fs.[31] We compared our dA response to the Drude spectrum calculated with these reported values in Supporting Information Figure S2b, and these values do not describe our dA response.

In comparison to the reported polaron mobility between 0.02 and 0.04 cm^2 V^{-1} s^{-1},[30,32] the free-carrier mobility differs significantly. As will be discussed in detail below and in agreement with previous TA spectroscopic assignments, our evidence suggests that the free-carrier mobility measured herein is related to free holes.

To support our hole effective mass findings, we have calculated the electron and hole effective masses using DFT. We perform our calculations in two steps (see Supporting Information). First, we optimize the lattice parameters using a hybrid functional, the HSE functional.[14] The lattice parameters computed with DFT−HSE are in excellent agreement with experiments (see Supporting Information).[33] We then compute band structures of m-BiVO$_4$ with DFT−GGA (see Supporting Information, Figure S3), from which the carrier effective masses, m_e^* and m_h^*, were computed, as presented in Supporting Information Table S2, along with comparisons to the existing literature.[34,35]

At the valence band maximum (VBM) (along the $\Gamma-V$ symmetry line) and the A point in the Brillouin zone, which are effectively degenerate within computational accuracy, the calculated hole effective mass is in good agreement with our experimentally determined value of $0.8m_e$. For the VBM and A, we compute $m_h^* = 0.734$ and $m_h^* = 0.795$ when approaching A from the M point, respectively. Note that the $\Gamma-V$ symmetry line has not been considered in previous works and leads to a smaller hole effective mass. However, for the conduction band minimum at the Z point, we find $m_e^* = 3.441$. Therefore, we conclude that the Drude optical response we observe in the TA data is related to band edge holes.

Thus far, we have identified spectral components related to ΔE_g and free carriers. However, these two spectral responses alone do not describe the large negative dA component (∼425 nm) that dominates the spectrum at early time delays. This feature has been previously assigned to bleaching of the ground state via the Burstein−Moss effect.[19−21] However, it is important to note that the experimentally observed bleach feature lies well above the fundamental absorption edge of BiVO$_4$, which has an indirect band gap of 2.5 eV (∼495 nm). As such, extremely high injection levels would be required to introduce a bleach feature near 425 nm, and it seems unlikely that band filling could be responsible for the observed spectral bleach. To test this hypothesis, we considered the role of state filling on the excited-state absorption coefficient, following the analysis of Yang et al.,[36] using our computed DFT joint density of states (JDOS) and excluding transitions related to the integral of the JDOS corresponding to the injected photo-carrier density. The excited-state carrier density was broadened by Fermi−Dirac statistics governing thermal excitations for a variety of carrier temperatures. The expected TA spectral line shape was taken as the difference between the excited-state JDOS and the ground-state JDOS. We found that this simple

approximation was unable to produce good agreement with the spectral line shapes of the dA experimental data, as shown in Supporting Information Figure S4, suggesting that state filling is not responsible for the significant negative dA feature observed in TA spectra of BiVO$_4$.

Given that state filling can be excluded as the origin of the pronounced bleach feature, we consider photoexcitation-induced broadening ($\Delta\Gamma$) of the absorption spectrum. Figure 3 shows a comparison between a calculated dA spectrum
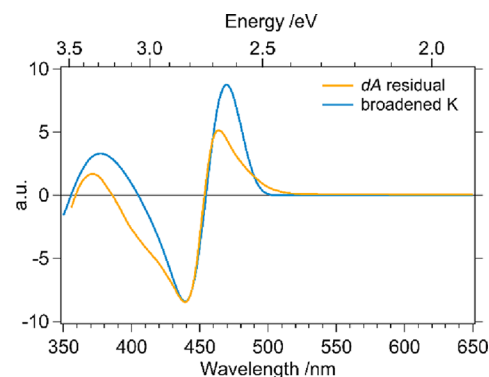

Figure 3. Residual of the transient differential absorption (dA) of BiVO$_4$, at 430 fs pump−probe delay, and the spectral components related to a change in the band gap and the photoexcited free carriers. This is compared to the difference spectrum of the ground state and Gaussian-broadened imaginary part of the complex refractive index.

obtained by Gaussian broadening of κ and the residual of the dA spectrum that is not accounted for by the ΔE_g and the Drude spectral components. We find that this energetic broadening approximation provides good agreement with the experimental residual. Broadening of optical transitions at high excitation or doping densities are often attributed to many-body effects because of the high concentration of carriers in their respective bands.[1,37] As can be seen in Supporting Information Figure S1b, by increasing the broadening magnitude, an increase in dA amplitude is expected with little change of the differential spectral line shapes. Therefore, the time variance of the $\Delta\Gamma$ component is related to relaxation of photoinduced carriers.

3.1.2. Thermal Contributions. Although TA spectroscopy experiments are most commonly aimed at understanding optoelectronic processes, illumination-induced sample heating can significantly affect measurements, as recently highlighted by the work of Hayes et al.[38] For example, with increasing temperature, thermal expansion leads to a shift of semiconductor band gap and phonon coupling leads to a broadening of the absorption edge. Accurate interpretation of the photoinduced electronic excited-state spectral response and its temporal evolution requires isolation of the non-electronic thermal components, though this is often overlooked. To evaluate spectral changes that may arise due to laser-induced sample heating, we first characterized steady-state transmission and reflection spectra of BiVO$_4$ films over a temperature range from 298 to 340 K. Figure 4a shows the differential transmission and reflection spectra, which are defined by dT, d$R = \log[I_{T,R}(T)/I_{T,R}(298 \text{ K})]$, acquired at a temperature of 340 K. From these spectra, the changes of optical absorption spectra as a function of temperature relative to 298 K were determined, as shown in Figure 4b. Derivative-like spectra are obtained, and remarkably, even a slight
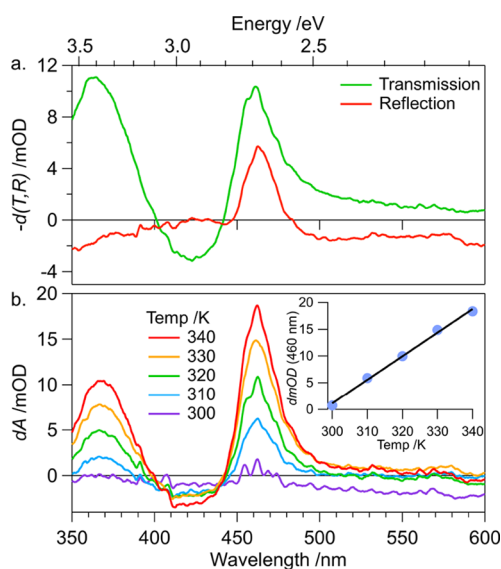
Figure 4. (a) Temperature difference (298 and 340 K) spectra taken in transmission and reflection geometry. (b) UV−vis temperature dependent difference absorption spectra taken at T_{hot} (indicated) and T_{298K}. (b, inset) Temperature dependence of the dA amplitude at 460 nm and the linear regression fit.

temperature increase of 2 K results in a measurable change in the optical density of ~1 mOD at 460 nm, which increases to ~19 mOD with a temperature increase of 42 K.

Striking similarities between the thermal difference spectra shown in Figure 4b and the spectra obtained from TA measurements on the same sample (Figure 2b) are observed. At early time delays (0.32−100 ps), the dA amplitude from TA measurements is significantly greater at 460 nm than at 360 nm. This amplitude difference diminishes up to 100 ps, after which the relative intensities are similar and decay together. Importantly, the dA spectrum obtained after 2000 ps and the thermal dA spectrum at 320 K (Supporting Information Figure S5) are nearly identical. These results, together with the analysis presented above, indicate that prior to 100 ps, there is a strong electronic component to the TA dA spectrum. However, at longer times, differential absorption spectra are dominated by thermal, rather than electronic, effects. This finding is important because slowly dissipating heat can easily be confused with long-lived electronic excitations and lead to erroneous correlations between TA data and functional characteristics of semiconductor light absorbers. Further discussion of the kinetics of these processes is provided below.

3.2. Modeling of the TA Spectral Time Dependence. By combining the physical descriptions of the various contributions to TA data, we fit complete experimental spectra at all time points and examine their kinetic evolution. The change of the absorption coefficient as a function of both photon energy and time, d$\alpha(E,t)$, is given by

$$d\alpha(\lambda) = \frac{4\pi}{\lambda}(d\kappa_{\Delta E_g} + d\kappa_\Gamma + \kappa_{Drude}) \tag{4}$$

with the change of the extinction coefficient from shifting of the band gap (d$\kappa_{\Delta E_g}$), broadening of the band gap (dκ_Γ), and Drude-like free-carrier absorption (κ_{Drude}) components. Equation 4 is related to the experimentally observed differential optical density (dOD) spectrum according to

$$dOD(\lambda) = -\log(e^{-Ld\alpha(\lambda)}) \tag{5}$$

where L is the film thickness. Thermal contributions to the optical spectra are included directly using the empirically determined thermal difference data (Figure 4b) and a time-dependent weighting function ($Q(t)$) given by

$$dOD(\lambda, t) = dOD(t) + Q(t)\, dOD_{thermal} \tag{6}$$

Figure 5a,b shows the experimental TA spectra after 0.43 ps and 2 ns, respectively, together with the individual fit
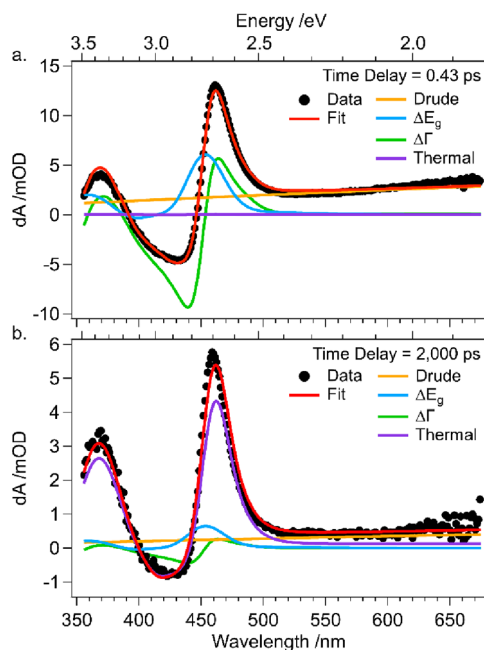

Figure 5. Differential absorption (dA) spectra at (a) 0.43 and (b) 2000 ps as excited by a 600 nJ pulse at 350 nm. The spectral components used in modeling the transient spectra are indicated related to a change of the band gap (ΔE_g), a change in band broadening ($\Delta\Gamma$), the free-carrier absorption (Drude), and the thermal contribution due to an increase in the lattice temperature (thermal). These are combined to produce the model as shown (Fit).

components (ΔE_g, $\Delta\Gamma$, Drude, and thermal) and the resulting envelope function. Both d$\kappa_{\Delta E_g}$ and dκ_Γ were calculated from the ground-state optical properties, as described above, and κ_{Drude} was calculated using eq 2. Excellent agreement between the fit model and experimental TA data is obtained at all time delays, ranging from the picosecond to the nanosecond ranges.

The complete time dependence of the normalized amplitude of each fitted spectral component is shown in Figure 6. For comparison, particularly at longer time delays, the experimental amplitude traces for probe wavelengths of 460 and 625 nm are also shown. The thermal contribution to the TA spectrum is not observed within the first 3 ps but then steadily rises and, after approximately 430 ps, plateaus. The time evolution of the lattice temperature was determined from the experimental temperature-dependent UV−vis data (Supporting Information Figure S6). For the case of 600 nJ excitation, the maximum increase in lattice temperature was approximately 5.4 K above room temperature. The ~10 ps delay of the thermal component dominance suggests that relaxation of hot photoexcited carriers occurs primarily through carrier/carrier
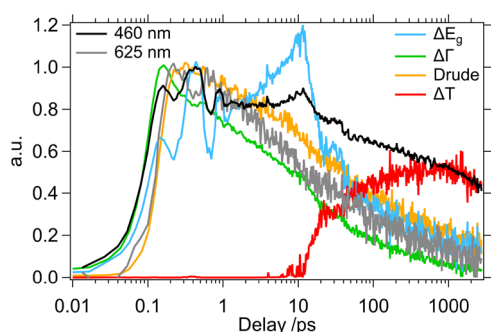
Figure 6. Time dependence of the fit components determined from the multicomponent spectral modeling. Traces are scaled for ease of visualization. The values of the free-carrier density and ΔE_g shift energy can be found in Supporting Information Figure S10a–c.

scattering. Carrier/lattice scattering and consequent dissipation to lattice heating appear to occur after the first 5–10 ps.

The ΔE_g, $\Delta \Gamma$, and Drude component signals decay rather quickly, within 10 ps, to approximately 50% of their initial amplitudes. The temporal response of these signals corresponds well with the 625 nm probe signal. The ΔE_g component is significantly different from the others in that it contains clear oscillatory behavior consistent with coherent optical and acoustic phonons, which will be discussed in more detail below. Very little oscillatory amplitude was seen in any of the others components. The existence of these features in the ΔE_g component is consistent with expectation, given the physical model of phonon-induced band gap modulation.

3.3. Coherent Phonon Contributions. Coherent phonon oscillations of $BiVO_4$, which appear as a modulation of the amplitude of transient pump–probe spectra, have been previously reported and provide insight into carrier–phonon interactions. In particular, using time-resolved terahertz spectroscopy, Butler et al. observed a 64 cm^{-1} component that they related to lattice distortions caused during hole polaron formation.[31] In the optical probe wavelength range, Ravensbergen et al. reported an intensity oscillation in the main induced absorption feature with a frequency of 63 cm^{-1}, which they assigned to a trapped hole coupled to a Raman-active phonon.[19] Aiga et al. observed a similar 62 cm^{-1} oscillation and assigned it to surface-trapped holes coupled to an external phonon mode involving vibrations of the Bi atoms.[17] Although the carrier-phonon coupling model is common to these reports, the exact origin of the signal in the visible range and its physical meaning are not yet well understood.

To gain further insights into carrier–phonon coupling and determine how such coupling manifests as a change of the dA amplitude, we performed differential transmission measurements over the temperature range from 11 to 373 K. Figure 7a shows the time dependence of dT, evaluated at 453 nm, for different temperatures. For ease of visualization, a linear plot of the first 5 ps is shown in Supporting Information Figure S7a. These data reveal several oscillatory components during the initial 100 ps, with coherence times that increase with decreased temperature. The highest frequency oscillations are well described by two damped sine functions with frequencies of ~105 and 64 ± 2 cm^{-1} at room temperature. We note that the ~105 cm^{-1} mode is challenging to fit accurately, given the time resolution of our instrument, but its inclusion is critical to describing the experimental data. Fitting the series of data
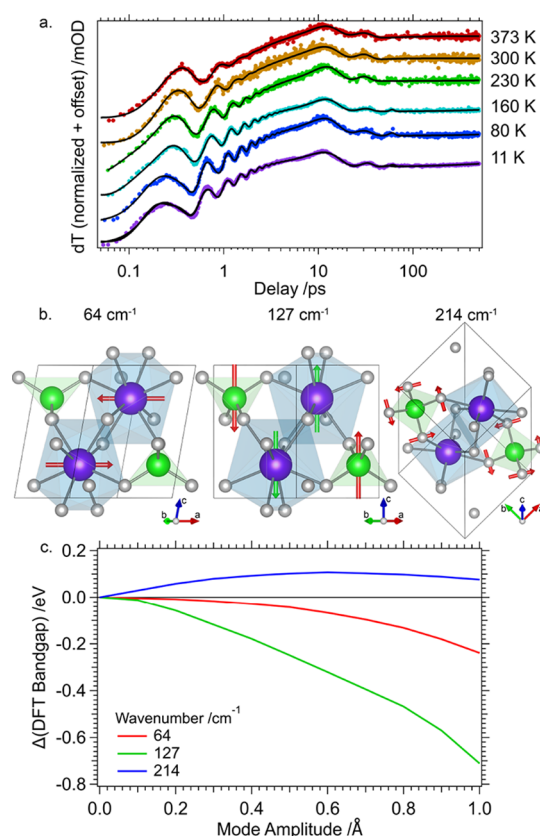

Figure 7. (a) Time dependence of the transient transmission data at a probe wavelength of 443 nm as a function of temperature highlighting the coherent phonon components in the data. (b) Visualization of vibrational modes of selected frequencies. Purple is bismuth-centered, green is vanadium-centered, and gray is oxygen located at the corners. The vibrational modes are denoted by red and green arrows. (c) Band gap variation versus vibrational mode amplitude for selected frequencies computed with the DFT–GGA exchange–correlation functional. The phonon mode amplitudes are computed with respect to normalized eigenvectors (see Supporting Information and Table S3 for details).

shown in Figure 7a, we extract an empirical model of the temperature dependence of the lower frequency component according to $\omega(T) = 78 \pm 2 - 5.5 \times 10^{-4} T^{1.77}$, as shown in Figure S7b. The temperature dependence of the phonon frequency is a consequence of anharmonicity.[39]

To elucidate the specific origin of these oscillations, we have computed zone-center phonon frequencies using DFT (see Supporting Information for details). Our calculated frequencies, shown in Figure 7b, are in good agreement with measured Raman spectra (see Supporting Information Figure S8) and the frequencies of oscillation within TA spectra. These are related to transverse optical (TO) and longitudinal optical (LO) modes with frequencies at 214 cm^{-1} (TO), 127 cm^{-1} (TO), 65 cm^{-1} (LO), and 64 cm^{-1} (TO) (see Supporting Information for details including Table S3 for a list of zone-center phonon frequencies). On the basis of these considerations, we conclude that the observed oscillations in the first few picoseconds arise from coherent optical phonons (COPs).

Although these COPs are evident in the TA data, the question of how they physically affect the amplitude of the dA spectrum remains. As described above, the principle components of the dA spectrum at early time delays are due to shifting and broadening of the band gap, as well as free-
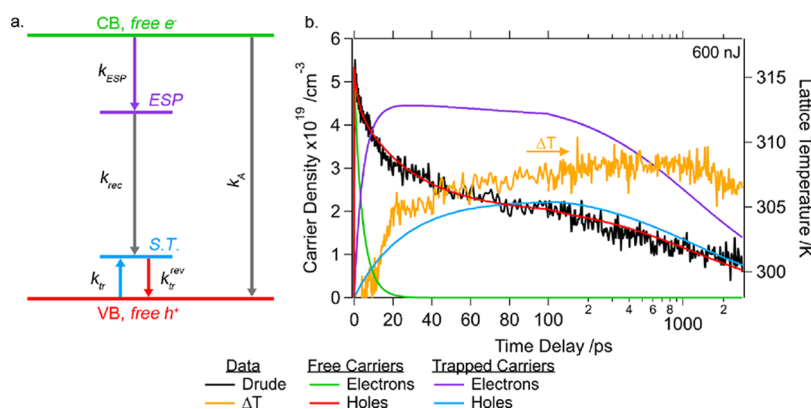
Figure 8. (a) Proposed kinetic model used for modeling the free-carrier density. Indicated are the related rate constants used in eqs 7–9. (b) Time dependence of the Drude component using 600 nJ excitation energy at 350 nm. From the kinetic modeling, the temporal behavior of the free electrons and trapped electrons and holes is calculated.

carrier absorption. Within this context, we note that coherent ionic displacement over a vibrational period induces time-variant changes of the band gap, which manifest as changes of the differential absorption intensity. To examine this more closely, we calculated the DFT band gap as a function of phonon mode amplitude for each of the three vibrational modes, as shown in Figure 7c. Although DFT band gaps are not expected to be quantitative, we expect their trends to be meaningful in this case. For the 127, 65, and 64 cm^{-1} modes, the DFT band gap decreases because of atomic motion, whereas the 214 cm^{-1} vibrational mode leads to atomic displacements that increase the band gap. Because the vibrational modes are excited coherently, band gap modulation is in phase and is observed in the measurement. Therefore, the oscillations are due to electron–phonon coupling of the excited carriers to the LO mode.

We assign the remaining features at >10 ps to coherent acoustic phonons (CAPs). First reported in the mid-1980s[40−42] and recently summarized in a review article by Ruello and Gusev,[43] CAPs in dR and dT measurements have been observed in metal oxide thin films such as Fe_2O_3.[44] In brief, optical excitation of the material by the pump pulse generates an elastic stress that results in a deformation potential. This deformation zone propagates as an acoustic pulse through the film and reflects off the interface with the substrate. The reflected wave can then interfere with incoming probe pulses at increased time delays with respect to the pump, thereby generating an oscillatory signal approximately proportional to two times the sample thickness divided by the speed of sound in the material. To provide additional confidence to this assignment, we examined several $BiVO_4$ film thicknesses, prepared by spin-coating, and found that this oscillation is temporally delayed with increasing the sample thickness, Supporting Information Figure S9.

The time dependence of CAP oscillations has been modeled using damped sine functions in some systems[45] and Gaussian functions in others.[46] Herein, we utilize Gaussian functions that provide good agreement to the data. In our sample, the emergence of the elastic stress volume due to thermal expansion is not instantaneous but rather delayed from the initial excitation event by a transfer of energy from electronically excited states to the lattice. As will be discussed below, this time dependence is in agreement with the time dependence of the extracted lattice temperature. We take the first peak at 11 ps to be the emergence of the excited volume

containing the elastic stress in the near surface region. The propagation of the strain front as a CAP, subsequent reflection off the back substrate, and return to the air/sample interface can be seen as the second inflection at 30 ps. Considering the sample thickness, we can approximate the speed of sound to be $1.4 \pm 0.2 \times 10^3$ m s^{-1}. Sound velocities have been reported for a $BiVO_4$ single crystal as a function of propagation directions and range from 1.6 to 4.9×10^3 m s^{-1} at room temperature,[47] in good agreement with our data. There is minimal temperature dependence to the sound velocity over the temperature range studied, which suggests that no phase transition or metal-to-insulator transition occurs. The latter has been observed in VO_2 and V_2O_5 at 350 and 150 K, respectively, by optical pump−probe and characterization of the photoacoustic temperature dependence[48] but is not present in $BiVO_4$ over the investigated temperature range.

3.4. Power Dependence and Kinetic Modeling. Several excitation powers, ranging from 90 to 800 nJ, were studied to gain insight into recombination mechanisms. The temporal evolution of N and ΔE_g as a function of excitation power are shown in Supporting Information Figure S10a,b. With an increase in fluence, a linear increase in free-carrier density and ΔE_g shift amplitude was observed, Supporting Information Figure S10c. The normalized traces of N, ΔE_g, and $\Delta\Gamma$ are given in Supporting Information Figure S11a−c. For the free-carrier density, an increase in the fast component amplitude was observed relative to the intensity of the long-lived tail at higher pump fluence, suggesting the presence of Auger recombination in this excitation regime. A similar trend is also observed in $\Delta\Gamma$, suggesting that the free-carrier density is related to band broadening, Supporting Information Figure S11c. For the ΔE_g component, no significant change in the temporal evolution of the normalized traces was observed.

The temporal behavior of the thermal component was similar for all pump powers over the entire excitation range, Supporting Information Figure S12. A maximum temperature change of 35 K was observed with 800 nJ excitation. A linear relationship between laser power and maximum lattice temperature was observed, as shown in the inset of Supporting Information Figure S12. We note that the contribution of the thermal component to the total signal is indeed significant, particularly at longer time delays, where it can almost completely describe the dA spectrum. Thus, it is critically important to account for thermal effects in the analysis of such TA spectra. Thermal dissipation is a naturally slow process and

can lead to erroneous assignments of persistent features to long-lived charge carriers. Furthermore, differences in thermal dissipation times for films grown on different substrates or immersed in water or other media should be carefully considered in the analysis of long-lived TA features.

Because the optical modeling presented above enables extraction of the temporal evolution of the free-carrier density, it was possible to develop a kinetic model based on the dynamics of this population density, as summarized in Figure 8a. The proposed model is consistent, in large part, with Suzuki et al.[22] This approach permits a level of physical insight that would not be possible in the absence of robust physical assignments of spectral features. Importantly, this also enables us to move beyond simple multiexponential fitting, which is not always clearly motivated from underlying physical origins. Our analysis methods enable simultaneous fitting of all excitation powers to one set of kinetic equations possessing a single set of kinetic rate constants.

From the kinetic modeling, we ascribe the free-carrier density to free holes. For the photoexcited electron density, we consider irreversible trapping into a deep trap state, in this case by formation of electron small polarons (ESPs). Carneiro et al. reported that small polaron formation in hematite occurred between 0.1 and 3 ps.[49] Consequently, we assert that the free-carrier signal modeled by the Drude function, which persists in our observations to 1000's of ps, is related to free-hole density. This assignment is consistent with previous reports utilizing electron and hole scavengers and applied bias in situ.[17−22] As previously discussed, we, and others,[31] have measured a free-carrier mobility several orders higher than the steady-state mobility governed by small polaron hopping. Therefore, the mobility we have measured is the hole mobility.

To model the evolution of the free-hole concentration, we consider a single shallow trap state with associated trapping and detrapping rate constants. Auger recombination is included in the fitting, though it is found that the npn mechanism was favored over pnp by the regression analysis. The differential equations describing these processes for the hole and electron concentrations with time are given by

$$-dp/dt = k_A n(pn - n_i^2) + k_{tr}p - k_{tr}^{rev}N_p^{tr} \qquad (7)$$

$$-dn/dt = k_A n(pn - n_i^2) + k_{ESP}n \qquad (8)$$

in which n and p are the free-electron and hole population densities, respectively, n_i is the intrinsic carrier concentration, N_p^{tr} is the concentration of shallow trapped holes, k_A is the Auger recombination rate constant, k_{tr} and k_{tr}^{rev} are the shallow hole trapping and detrapping rate constants, respectively, and k_{ESP} is the ESP formation rate constant. Although the effective densities of states of the valence and conduction band are not known for BiVO$_4$, use of reasonable values, on the order of those of Si, results in small values for n_i that do not significantly affect fitting results. Recombination of the shallow trapped holes with ESPs, governed by the rate constant k_{rec}, is given by

$$-dN_p^{tr}/dt = k_{rec}N_{ESP}N_p^{tr} - k_{tr}p + k_{tr}^{rev}N_p^{tr} \qquad (9)$$

Fitting of the experimental data yields values of $k_A = 3.2 \times 10^{-41}$ (cm^{-3})$^{-2}$ ps^{-1}, $k_{tr} = 1.9 \times 10^{-2}$ ps^{-1}, $k_{tr}^{rev} = 1.6 \times 10^{-2}$ ps^{-1}, $k_{ESP} = 0.20$ ps^{-1}, and $k_{rec} = 3.4 \times 10^{-23}$ (cm^{-3})$^{-1}$ ps^{-1}. The error on the rate constants is approximately 20%.

The relative closeness of the k_{tr} and k_{tr}^{rev} rates suggests that the hole trap is close to the valence band edge, possibly within

kT. This observation is consistent with our previous report on the temperature dependence of deep level trap state luminescence, in which we observed a 41 ± 2 meV activation barrier to thermal quenching of the PL intensity.[50] Since that time, Ziwritsch reported evidence for a hole polaron with hopping activation energy of ∼90 meV.[32] Taken together, these results suggest that a dynamic equilibrium of free holes and hole polarons exists in the material.

The temporal response of the kinetic model for the 600 nJ excitation energy is shown in Figure 8b. The response of the free-hole density was used to model the Drude signal for which we have achieved excellent agreement across all excitation powers studied (see Figure S13), with the only adjustable parameter being the initial free-carrier density. Additionally, illustrated in Figure 8b are the modeled population densities related to the free electron and trapped electrons/holes. Interestingly, the trapped hole density rise matches surprisingly well with the time dependence of the lattice temperature. Although we cannot draw a decisive correlation between hole trapping and lattice temperature, this relationship in the model may be of further interest for follow-up studies.

Kinetic modeling of the ΔE_g shift energy and $\Delta \Gamma$ amplitude is made challenging because of the potential for convoluted spectral overlap from multiple physical origins. As we have described previously, the ΔE_g parameter could contain influences from a variety of phenomena related to band gap renormalization from the free-hole density, polaronic changes, or otherwise. Likewise, the influence from multiple processes could convolute the $\Delta \Gamma$ parameter. Furthermore, the kinetic model and related rate constants were constructed on the basis of free-hole density, whereas the ΔE_g and $\Delta \Gamma$ signals are known only in units of millielectron volts and a unitless scalar. To be able to utilize the model to fit these components, we have assumed that the ΔE_g and $\Delta \Gamma$ signals at a given excitation power can be related back to the free-carrier density at $t = 0$ s and, as such, normalized them to the Drude extracted carrier density. Furthermore, to account for signals originating from the various population densities, we used a linear combination method (LCM) combining free-electron, free-hole, trapped hole, and ESP population densities to fit the experimental data. For ΔE_g, we also included two damped sines and three Gaussian functions to be able to model features related to the COP and CAP, respectively. The damped sine frequencies were 105 and 64 cm^{-1}. The CAP peaks were centered at 11.6 ± 0.5, 32 ± 1, and 60 ± 2 ps. The sound velocities would be $1.3 \times 10^3 \pm 0.2 \times 10^3$ m s^{-1} and $1.6 \times 10^3 \pm 0.2 \times 10^3$ m s^{-1} if we assume full round trips through the 53 nm thick sample.

Using the LCM approach, we could reproduce the ΔE_g and $\Delta \Gamma$ signals using the model components across all excitation powers, as shown in Figure S14. For the ΔE_g signal at 600 nJ excitation energy, the LCM resulted in excellent agreement using free-electron and trapped electron population densities. For the $\Delta \Gamma$ component, the LCM analysis using the free-hole and free-electron population densities resulted in the best quality fit. Further analysis is required to relate these substituent kinetic components to the material performance as a photoelectrode. However, our approach provides a path forward to better understanding these complex phenomena.

4. CONCLUSIONS

Thin-film m-BiVO$_4$ was studied by TA spectroscopy over the first 2.5 ns after photoexcitation. Both transient transmission and reflection spectra were co-collected to generate the true

differential absorption (dA) spectra. At early time delays, the principle dA components were related to shifting and broadening of the ground-state optical properties, consistent with other forms of modulation spectroscopies. In addition, free-carrier absorption was well described by the Drude model enabling the extraction of the free-hole effective mass and mobility. Starting at 10 ps and plateauing after ~200 ps, the thermal modifications to the optical properties introduced by heating from the optical pumping contributed significantly to the transient spectra. Deconvolution of the dA spectra into shifting, broadening, free-carrier, and thermal components was achieved for all time delays. Optically excited lattice mode phonons were evident in the band shifting channel, which was related to modulation of the optical band gap during the period of oscillation. CAPs were also evident in the band shifting channel and are related to propagation of an acoustic wave front through the thickness of the film. From the temporal evolution of the free-carrier density, we were able to construct a kinetic model of recombination based on Auger recombination, ESP formation, shallow hole trapping and detrapping, and eventual recombination between the electron polaron and trapped holes. The kinetic model was trained on several photoinjected carrier densities ranging from 8×10^{18} to 7×10^{19} cm^{-3} from which we extract kinetic rate constants. Through linear combination fitting of the model constituent population densities, the band shifting and broadening kinetics could also be well described. This work provides significantly improved understanding of fundamental processes governing carrier dynamics and recombination kinetics in a prototypical thin-film light absorber. More generally, our approach to modeling the dA spectra based on electronic and thermal modulation of ground-state optical properties provides a new perspective to analysis of TA spectra of a wide variety of semiconductor thin films.

ASSOCIATED CONTENT

Ⓢ Supporting Information

The Supporting Information is available free of charge on the ACS Publications website at DOI: 10.1021/acs.jpcc.8b06645.

Discussion of DFT methods and computational unit cell, band effective masses, band structure, and vibrational mode frequencies; derivation of the differential absorption equation used to combine dR and dT; Example differential spectra based on shifting and broadening; Drude spectral analysis for several values of m^*; optical modeling of state filling; thermal difference spectra compared to dA at 2000 ps; maximum lattice temperature versus pump energy and the temporal evolution of the lattice temperature; coherent phonons measured in dT for several sample temperatures and fitting of the temperature dependence of the vibrational mode frequency; Raman spectrum; CAP signals for several sample thicknesses; excitation energy dependence of the temporal evolution of the free-carrier density and ΔE_g components with linear regression for the signal amplitudes versus pump energy; normalized temporal behavior for the excitation dependence of the model components; and kinetic model fit of the excitation energy dependence of the free-hole density, ΔE_g, and $\Delta \Gamma$ (PDF)

AUTHOR INFORMATION

Corresponding Authors

*E-mail: jkcooper@lbl.gov (J.K.C.).
*E-mail: sharp@wsi.tum.de (I.D.S.).

ORCID Ⓘ

Jason K. Cooper: 0000-0002-7953-4229
Ian D. Sharp: 0000-0001-5238-7487

Notes

The authors declare no competing financial interest.

REFERENCES

(1) Schultze, M.; Ramasesha, K.; Pemmaraju, C. D.; Sato, S. A.; Whitmore, D.; Gandman, A.; Prell, J. S.; Borja, L. J.; Prendergast, D.; Yabana, K.; et al. Attosecond band-gap dynamics in silicon. *Science* **2014**, *346*, 1348−1352.

(2) Pendlebury, S. R.; Barroso, M.; Cowan, A. J.; Sivula, K.; Tang, J.; Grätzel, M.; Klug, D.; Durrant, J. R. Dynamics of photogenerated holes in nanocrystalline α-Fe2O3electrodes for water oxidation probed by transient absorption spectroscopy. *Chem. Commun.* **2011**, *47*, 716−718.

(3) Pollak, F. H.; Shen, H. Modulation spectroscopy of semiconductors: bulk/thin film, microstructures, surfaces/interfaces and devices. *Mater. Sci. Eng., R* **1993**, *10*, 275−374.

(4) Yang, Y.; Gu, J.; Young, J. L.; Miller, E. M.; Turner, J. A.; Neale, N. R.; Beard, M. C. Semiconductor interfacial carrier dynamics via photoinduced electric fields. *Science* **2015**, *350*, 1061−1065.

(5) Jeon, T. H.; Choi, W.; Park, H. Cobalt-phosphate complexes catalyze the photoelectrochemical water oxidation of BiVO4 electrodes. *Phys. Chem. Chem. Phys.* **2011**, *13*, 21392−21401.

(6) Lichterman, M. F.; Shaner, M. R.; Handler, S. G.; Brunschwig, B. S.; Gray, H. B.; Lewis, N. S.; Spurgeon, J. M. Enhanced stability and activity for water oxidation in alkaline media with bismuth vanadate photoelectrodes modified with a cobalt oxide catalytic layer produced by atomic layer deposition. *J. Phys. Chem. Lett.* **2013**, *4*, 4188−4191.

(7) Cooper, J. K.; Gul, S.; Toma, F. M.; Chen, L.; Liu, Y.-S.; Guo, J.; Ager, J. W.; Yano, J.; Sharp, I. D. Indirect bandgap and optical properties of monoclinic bismuth vanadate. *J. Phys. Chem. C* **2015**, *119*, 2969−2974.

(8) Bakke, J. R.; Hägglund, C.; Jung, H. J.; Sinclair, R.; Bent, S. F. Atomic layer deposition of CdO and CdxZn1−xO films. *Mater. Chem. Phys.* **2013**, *140*, 465−471.

(9) Khoshman, J. M.; Hilfiker, J. N.; Tabet, N.; Kordesch, M. E. Multiple oscillator models for the optical constants of polycrystalline zinc oxide thin films over a wide wavelength range. *Appl. Surf. Sci.* **2014**, *307*, 558−565.

(10) Kresse, G.; Furthmüller, J. Efficient iterative schemes forab initiototal-energy calculations using a plane-wave basis set. *Phys. Rev. B: Condens. Matter Mater. Phys.* **1996**, *54*, 11169−11186.

(11) Perdew, J. P.; Burke, K.; Ernzerhof, M. Generalized gradient approximation made simple. *Phys. Rev. Lett.* **1996**, *77*, 3865−3868.

(12) Blöchl, P. E. Projector augmented-wave method. *Phys. Rev. B: Condens. Matter Mater. Phys.* **1994**, *50*, 17953−17979.

(13) Kresse, G.; Joubert, D. From ultrasoft pseudopotentials to the projector augmented-wave method. *Phys. Rev. B: Condens. Matter Mater. Phys.* **1999**, *59*, 1758−1775.

(14) Krukau, A. V.; Vydrov, O. A.; Izmaylov, A. F.; Scuseria, G. E. Influence of the exchange screening parameter on the performance of screened hybrid functionals. *J. Chem. Phys.* **2006**, *125*, 224106.

(15) Baroni, S.; Giannozzi, P.; Testa, A. Green's-function approach to linear response in solids. *Phys. Rev. Lett.* **1987**, *58*, 1861−1864.

(16) Momma, K.; Izumi, F. VESTA 3for three-dimensional visualization of crystal, volumetric and morphology data. *J. Appl. Crystallogr.* **2011**, *44*, 1272−1276.

(17) Aiga, N.; Jia, Q.; Watanabe, K.; Kudo, A.; Sugimoto, T.; Matsumoto, Y. Electron-Phonon Coupling Dynamics at Oxygen Evolution Sites of Visible-Light-Driven Photocatalyst: Bismuth Vanadate. *J. Phys. Chem. C* **2013**, *117*, 9881−9886.

(18) Ma, Y.; Pendlebury, S. R.; Reynal, A.; Le Formal, F.; Durrant, J. R. Dynamics of photogenerated holes in undoped BiVO4 photo-anodes for solar water oxidation. *Chem. Sci.* **2014**, *5*, 2964−2973.

(19) Ravensbergen, J.; Abdi, F. F.; van Santen, J. H.; Frese, R. N.; Dam, B.; van de Krol, R.; Kennis, J. T. M. Unraveling the Carrier Dynamics of BiVO4: A Femtosecond to Microsecond Transient Absorption Study. *J. Phys. Chem. C* **2014**, *118*, 27793−27800.

(20) Grigioni, I.; Stamplecoskie, K. G.; Selli, E.; Kamat, P. V. Dynamics of Photogenerated Charge Carriers in WO3/BiVO4 Heterojunction Photoanodes. *J. Phys. Chem. C* **2015**, *119*, 20792−20800.

(21) Pattengale, B.; Ludwig, J.; Huang, J. Atomic Insight into the W-Doping Effect on Carrier Dynamics and Photoelectrochemical Properties of BiVO4 Photoanodes. *J. Phys. Chem. C* **2016**, *120*, 1421−1427.

(22) Suzuki, Y.; Murthy, D. H. K.; Matsuzaki, H.; Furube, A.; Wang, Q.; Hisatomi, T.; Domen, K.; Seki, K. Rational Interpretation of Correlated Kinetics of Mobile and Trapped Charge Carriers: Analysis of Ultrafast Carrier Dynamics in BiVO4. *J. Phys. Chem. C* **2017**, *121*, 19044−19052.

(23) Cooper, J. K.; Gul, S.; Toma, F. M.; Chen, L.; Glans, P.-A.; Guo, J.; Ager, J. W.; Yano, J.; Sharp, I. D. Electronic Structure of Monoclinic BiVO4. *Chem. Mater.* **2014**, *26*, 5365−5373.

(24) Aspnes, D. E. Third-derivative modulation spectroscopy with low-field electroreflectance. *Surf. Sci.* **1973**, *37*, 418−442.

(25) Cerdeira, F.; Cardona, M. Photoreflectance and electro-reflectance in silicon. *Solid State Commun.* **1969**, *7*, 879−882.

(26) Hwang, E. H.; Das Sarma, S. Band-gap renormalization in photoexcited semiconductor quantum-wire structures in theGWap-proximation. *Phys. Rev. B: Condens. Matter Mater. Phys.* **1998**, *58*, R1738−R1741.

(27) Klingshirn, C. Properties of the electron-hole plasma in II−VI semiconductors. *J. Cryst. Growth* **1992**, *117*, 753−757.

(28) Güven, K.; Tanatar, B. Phonon renormalization effects in photoexcited quantum wires. *Phys. Rev. B: Condens. Matter Mater. Phys.* **1995**, *51*, 1784−1790.

(29) Rettie, A. J. E.; Lee, H. C.; Marshall, L. G.; Lin, J.-F.; Capan, C.; Lindemuth, J.; McCloy, J. S.; Zhou, J.; Bard, A. J.; Mullins, C. B. Combined Charge Carrier Transport and Photoelectrochemical Characterization of BiVO4 Single Crystals: Intrinsic Behavior of a Complex Metal Oxide. *J. Am. Chem. Soc.* **2013**, *135*, 11389−11396.

(30) Abdi, F. F.; Savenije, T. J.; May, M. M.; Dam, B.; van de Krol, R. The Origin of Slow Carrier Transport in BiVO4 Thin Film Photoanodes: A Time-Resolved Microwave Conductivity Study. *J. Phys. Chem. Lett.* **2013**, *4*, 2752−2757.

(31) Butler, K. T.; Dringoli, B. J.; Zhou, L.; Rao, P. M.; Walsh, A.; Titova, L. V. Ultrafast carrier dynamics in BiVO4 thin film photoanode material: interplay between free carriers, trapped carriers and low-frequency lattice vibrations. *J. Mater. Chem. A* **2016**, *4*, 18516−18523.

(32) Ziwritsch, M.; Müller, S.; Hempel, H.; Unold, T.; Abdi, F. F.; van de Krol, R.; Friedrich, D.; Eichberger, R. Direct Time-Resolved Observation of Carrier Trapping and Polaron Conductivity in BiVO4. *ACS Energy Lett.* **2016**, *1*, 888−894.

(33) Sleight, A. W.; Chen, H.-y.; Ferretti, A.; Cox, D. E. Crystal growth and structure of BiVO4. *Mater. Res. Bull.* **1979**, *14*, 1571−1581.

(34) Ding, K.; Chen, B.; Fang, Z.; Zhang, Y. Density functional theory study on the electronic and optical properties of three crystalline phases of BiVO4. *Theor. Chem. Acc.* **2013**, *132*, 1352.

(35) Zhao, Z.; Li, Z.; Zou, Z. Electronic structure and optical properties of monoclinic clinobisvanite BiVO4. *Phys. Chem. Chem. Phys.* **2011**, *13*, 4746−4753.

(36) Yang, Y.; Ostrowski, D. P.; France, R. M.; Zhu, K.; van de Lagemaat, J.; Luther, J. M.; Beard, M. C. Observation of a hot-phonon bottleneck in lead-iodide perovskites. *Nat. Photonics* **2016**, *10*, 53−59.

(37) Viña, L.; Cardona, M. Effect of heavy doping on the optical properties and the band structure of silicon. *Phys. Rev. B: Condens. Matter Mater. Phys.* **1984**, *29*, 6739−6751.

(38) Hayes, D.; Hadt, R. G.; Emery, J. D.; Cordones, A. A.; Martinson, A. B. F.; Shelby, M. L.; Fransted, K. A.; Dahlberg, P. D.; Hong, J.; Zhang, X.; et al. Electronic and nuclear contributions to time-resolved optical and X-ray absorption spectra of hematite and insights into photoelectrochemical performance. *Energy Environ. Sci.* **2016**, *9*, 3754−3769.

(39) Irmer, G.; Wenzel, M.; Monecke, J. The temperature dependence of the LO(T) and TO(T) phonons in GaAs and InP. *Phys. Status Solidi B* **1996**, *195*, 85−95.

(40) Thomsen, C.; Strait, J.; Vardeny, Z.; Maris, H. J.; Tauc, J.; Hauser, J. J. Coherent phonon generation and detection by picosecond light pulses. *Phys. Rev. Lett.* **1984**, *53*, 989−992.

(41) Tam, A. C. Applications of photoacoustic sensing techniques. *Rev. Mod. Phys.* **1986**, *58*, 381−431.

(42) Thomsen, C.; Grahn, H. T.; Maris, H. J.; Tauc, J. Surface generation and detection of phonons by picosecond light pulses. *Phys. Rev. B: Condens. Matter Mater. Phys.* **1986**, *34*, 4129−4138.

(43) Ruello, P.; Gusev, V. E. Physical mechanisms of coherent acoustic phonons generation by ultrafast laser action. *Ultrasonics* **2015**, *56*, 21−35.

(44) Joly, A. G.; Williams, J. R.; Chambers, S. A.; Xiong, G.; Hess, W. P.; Laman, D. M. Carrier dynamics in α-Fe2O3 (0001) thin films and single crystals probed by femtosecond transient absorption and reflectivity. *J. Appl. Phys.* **2006**, *99*, 053521.

(45) Ge, S.; Liu, X.; Qiao, X.; Wang, Q.; Xu, Z.; Qiu, J.; Tan, P.-H.; Zhao, J.; Sun, D. Coherent longitudinal acoustic phonon approaching THz frequency in multilayer molybdenum disulphide. *Sci. Rep.* **2014**, *4*, 5722.

(46) Saito, T.; Matsuda, O.; Wright, O. Picosecond acoustic phonon pulse generation in nickel and chromium. *Phys. Rev. B: Condens. Matter Mater. Phys.* **2003**, *67*, 205421.

(47) Avakyants, L. P.; Chervyakov, A. V.; Gorelik, V. S.; Sverbil', P. P. Inelastic light scattering near the ferroelectric phase-transition point in bismuth vanadate crystals. *J. Russ. Laser Res.* **2004**, *25*, 535−580.

(48) Abreu, E.; Gilbert Corder, S. N.; Yun, S. J.; Wang, S.; Ramírez, J. G.; West, K.; Zhang, J.; Kittiwatanakul, S.; Schuller, I. K.; Lu, J.; et al. Ultrafast electron-lattice coupling dynamics in VO2 and V2O3 thin films. *Phys. Rev. B: Condens. Matter Mater. Phys.* **2017**, *96*, 094309.

(49) Carneiro, L. M.; Cushing, S. K.; Liu, C.; Su, Y.; Yang, P.; Alivisatos, A. P.; Leone, S. R. Excitation-wavelength-dependent small polaron trapping of photoexcited carriers in α-Fe2O3. *Nat. Mater.* **2017**, *16*, 819−825.

(50) Cooper, J. K.; Scott, S. B.; Ling, Y.; Yang, J.; Hao, S.; Li, Y.; Toma, F. M.; Stutzmann, M.; Lakshmi, K. V.; Sharp, I. D. Role of Hydrogen in Defining the n-Type Character of BiVO4 Photoanodes. *Chem. Mater.* **2016**, *28*, 5761−5771.